Contents lists available at ScienceDirect

Circular Economy

CIRCULAR ECONOMY

Original Research

Malachite green dye removal with aluminosilicate nanopowder from aluminum dross and silicomanganese slag

Check for updates

Mostafa Mahinroosta [a, b, *], Rozita M Moattari [c], Ali Allahverdi [b], Pooria Ghadir [d, e]

[a] Department of Energy, Materials and Energy Research Center, Karaj 3177983634, Iran
[b] Research Laboratory of Inorganic Chemical Process Technologies, School of Chemical Engineering, Iran University of Science and Technology, Narmak 1684613114, Tehran, Iran
[c] Center of Excellence for Membrane Science and Technology, Department of Chemical, Petroleum and Gas Engineering, Iran University of Science and Technology (IUST), Narmak 1684613114, Tehran, Iran
[d] Department of Civil and Environmental Engineering, University of Strathclyde, Glasgow G1 1XJ, UK
[e] Department of Engineering, University of Exeter, Exeter EX4 4QF, UK

ABSTRACT

Malachite green is a persistent, bioaccumulative, mutagenic, carcinogenic, and teratogenic dye that poses significant risks in water sources, making its removal from water a critical necessity. This study aims to fabricate a sorbent comprising amorphous aluminosilicate nanopowder utilizing silicomanganese slag (SMS) and secondary aluminum dross (SAD) waste materials to remediate dye-contaminated water. The silica and alumina components of the SMS and SAD were extracted as sodium silicate and sodium aluminate leachates, respectively, through an effective hydrometallurgical conversion process. An empirical formula of $Al_2O_3 \cdot 2.3SiO_2$ was deduced from the X-ray fluorescence analysis of the synthesized material. The X-ray diffraction (XRD) pattern indicated the amorphous nature of the synthesized aluminosilicate, with no evidence of nanocrystals or ordered clusters observed via high-resolution transmission electron microscopy (TEM). Based on TEM micrographs, the aluminosilicate particles ranged in size from 20 to 80 nm. The synthesized aluminosilicate nanopowder was utilized to treat wastewater containing malachite green dye, demonstrating a remarkable dye removal efficiency of 97% after a 15-min contact time using 30 mg of adsorbent in a 30 mL dye solution at 200 rpm. The methodology proposed in this study could facilitate the production of amorphous aluminosilicate powder as a high-value product from industrial waste. Studies on its reusability demonstrated that it could remove over 90% of the dye after three cycles of use.

1. Introduction

Today, conserving and rejuvenating groundwater has become increasingly crucial. Researchers are continuously exploring cost-effective approaches to restore groundwater and enhance water quality. Among these, the adsorption process excels owing to its utilization of efficient and economical sorbents. Synthesizing effective adsorbents from industrial waste not only reduces surface water contamination but also enhances water quality. Aluminosilicates, as inorganic composites, possess exceptional characteristics that render them ideal for water purification. Their ion-exchange capability, high surface area, shape-selectivity, and thermal/ hydrothermal stability make them suitable for various applications, particularly in wastewater treatment (Lopes et al., 2014).

Inorganic nanoparticles have been synthesized through various techniques, including sol−gel (Naderi-Beni & Alizadeh, 2020), hydrothermal method (Fu et al., 2019), sonochemical (Lopes et al., 2014), solvothermal (Fotukian et al., 2020), homogeneous precipitation (Kant Sharma et al., 2017), reverse micelles (Thakur et al., 2009), nonhydrolytic (Leidich et al., 2016), flame spray pyrolysis (Meng & Zhao, 2020), thermal evaporation (Rehman et al., 2019), mechanochemical (Duan et al., 2019), and solution combustion synthesis (Liu et al., 2019) methods. Among these, the sol−gel process has recently been employed to synthesize high-purity nanostructured aluminosilicate (Akhlaghian et al., 2014; Pereira et al., 2019; Zheng et al., 2012). Here, nanosized aluminosilicate powder was synthesized using aluminum tri-sec-butoxide and tetraethyl orthosilicate (TEOS) (Pereira et al., 2019). Additionally, nanosized aluminosilicate powder was synthesized from TEOS and

---

* Corresponding author. Department of Energy, Materials and Energy Research Center, Karaj 3177983634, Iran.
E-mail address: mahinroosta2010@gmail.com (M. Mahinroosta).

aluminum nitrate using the sol−gel method combined with azeotropic distillation (Zheng et al., 2012).

Scaling up the production of nanosized aluminosilicate for commercial purposes is hampered by the high cost associated with using pure-grade salts in the synthesis process. Therefore, lowering production costs could significantly broaden the applications of these nanocomposites, enhancing their versatility due to their advantageous properties. Recently, the concept of recycling industrial solid waste has emerged as a viable solution to reduce production expenses, mitigate the depletion of natural resources, and tackle environmental issues linked to waste disposal (Mahinroosta & Allahverdi, 2018a).

Silicomanganese slag (SMS) is the primary byproduct of manganese ferroalloy plants generated during the production of manganese-steel pig iron (Choi et al., 2017). Approximately 1.2−1.4 tons of SMS are produced per ton of SiMn alloy, with global production estimated at 8−10 million tons annually

(Kumar et al., 2013). The disposal of large quantities of SMS in open areas poses environmental challenges and contributes to natural resource depletion (Frías et al., 2009; Kim et al., 2011). Notably, SMS is utilized in various applications, such as road subbase filler, railway ballast, substitute for Portland cement, and manufacturing of glass ceramics, alkali-activated cement, and geopolymers (Najamuddin et al., 2019; Zhuang et al., 2016). In recycling, alkali-activated cement has attracted considerable interest due to its eco-friendly attributes, including low energy consumption, reduced greenhouse gas emissions, and exceptional durability (Nath & Kumar, 2019; Zhang et al., 2018). For example, SMS has been employed as an additive to enhance the mechanical strength of fly ash-based geopolymers by forming a calcium-rich hydrated product at room temperature (Mahinroosta & Allahverdi, 2018a). Additionally, alkali-activated SMS-based materials incorporating carbon black show promise for removing dye pollutants (Zhang et al., 2018).
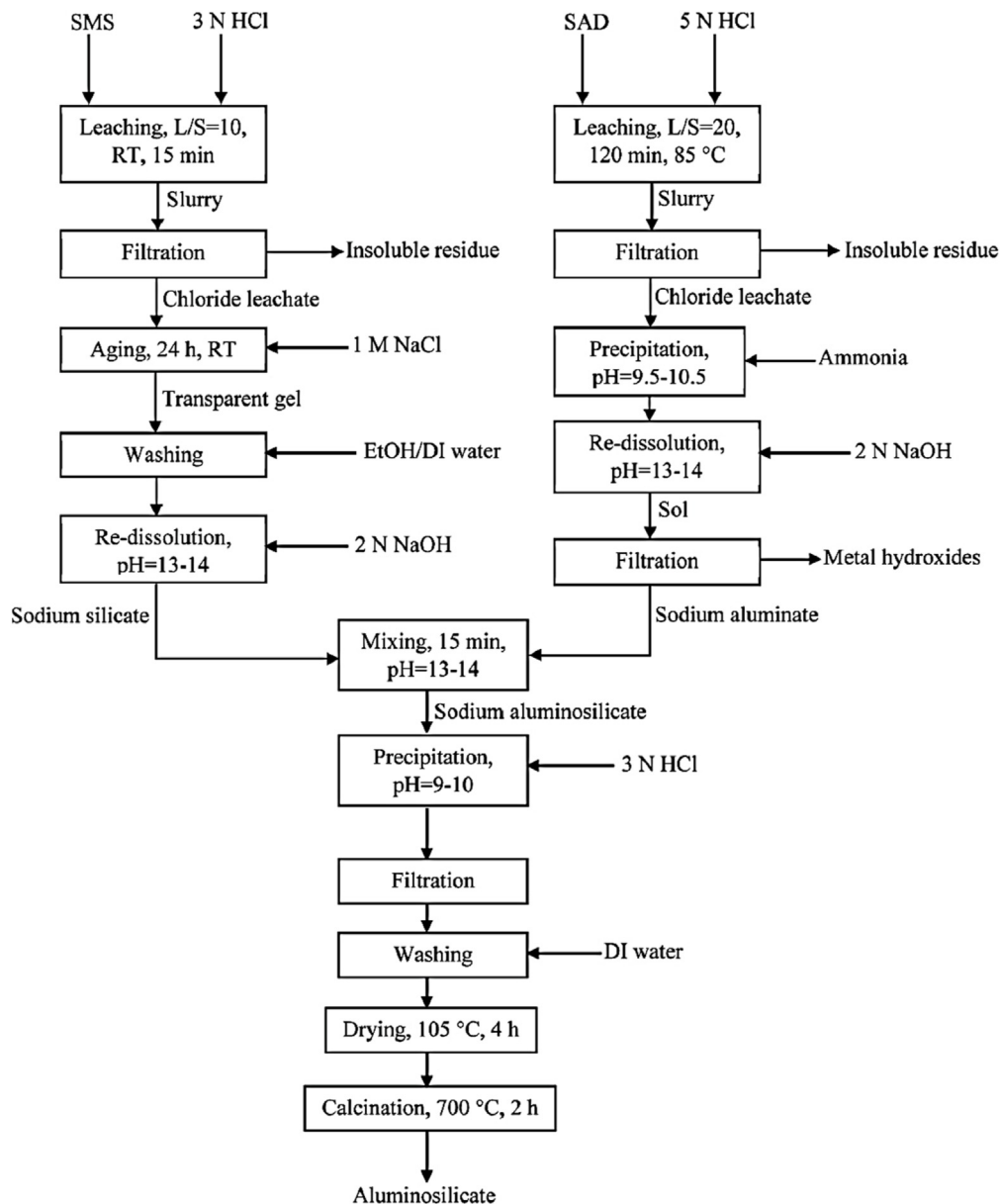

Fig. 1. Flow diagram for synthesis of aluminosilicate from SAD and SMS.

Table 1
Chemical composition of secondary aluminum dross (SAD) and silicomanganese slag (SMS) (wt.%).

Element	SAD	SMS
Si	12.4	29.9
Ca	4.3	35.1
Al	55.2	13.1
Mn	0.5	13.4
MgO	—	2.9
Fe	7.6	2.1
K	1.3	1.1
Na	3.4	0.5
S	0.2	0.1
Ti	0.4	—
Cu	0.3	—
Cr	0.028	0.015
Zn	0.216	0.315
Ni	0.037	0.078

The SMS, a rich source of silica and manganese, offers vast potential for producing silica-based products, such as nanosilica for wastewater treatment adsorbents (Namvar et al., 2021, 2023) and silica aerogel (Namvar et al., 2022), as well as manganese-based

products. Notably, studies on SMS valorization are significantly limited, and this study can initiate a new era of research in this field.

Aluminum dross, an industrial byproduct, presents significant hazards to public health. Typically, 15−25 kg of dross is generated when 100 kg of aluminum is melted in the aluminum production sector (Mahinroosta & Allahverdi, 2018a). This waste material can be categorized based on its chemical composition and appearance. Primary dross, in a clustered form, contains around 40−50 wt% metallic aluminum, while secondary dross, typically granular, contains less than 20 wt% metallic aluminum (Mahinroosta & Allahverdi, 2018a). Methods for managing aluminum dross include extracting alpha and gamma alumina, producing construction materials, and utilizing separation agents (Mahinroosta and Allahverdi, 2020, 2021; Mohammadzadeh et al., 2022). With alumina content ranging from 40 to 70 wt%, large-scale alumina extraction may become economically viable, necessitating further research.

This study's use of two industrial wastes—secondary aluminum dross (SAD) and SMS—offers multiple advantages simultaneously. First, it provides a solution for mitigating their environmental impact. Second, it prevents the loss of valuable components in their
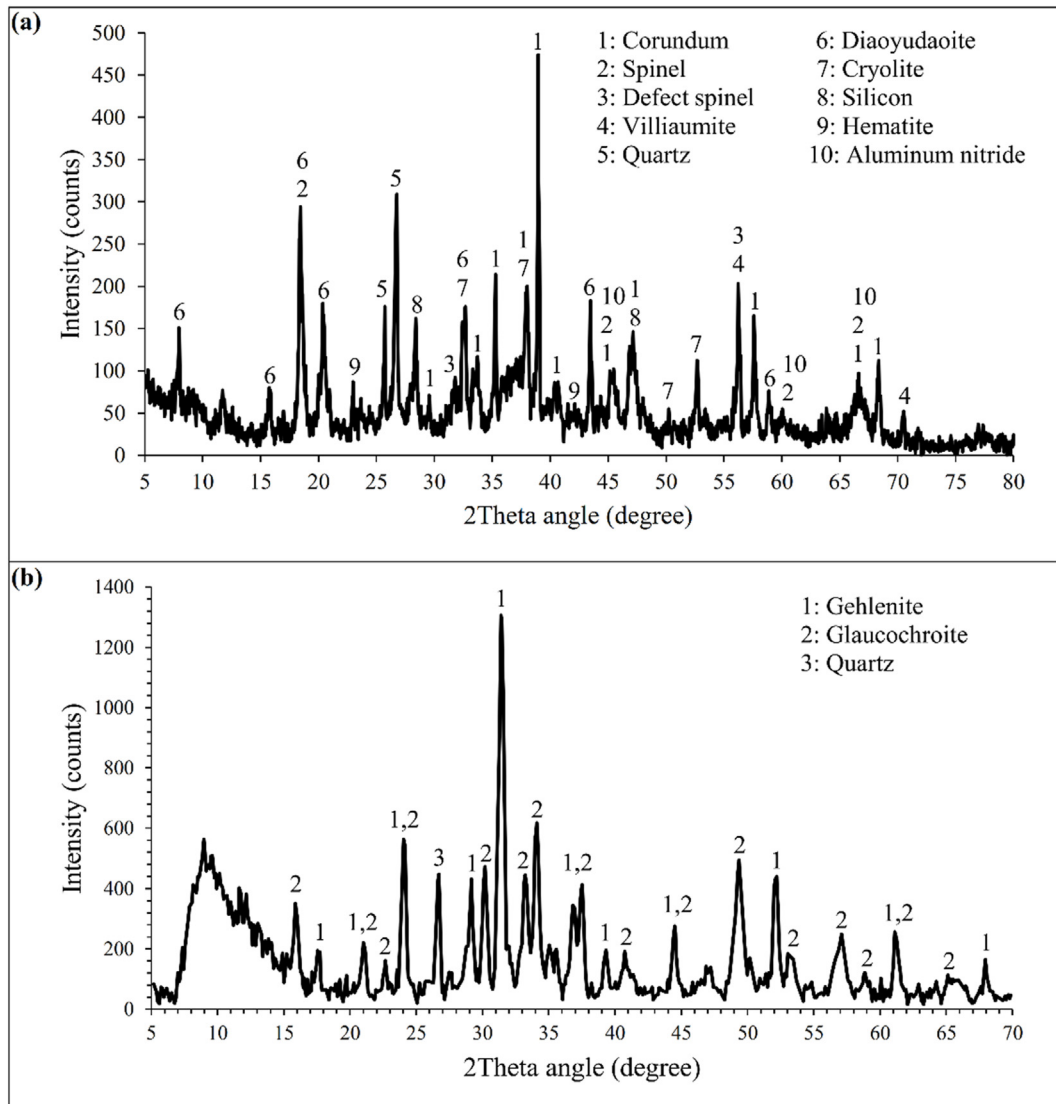

Fig. 2. XRD patterns of (a) SAD and (b) SMS.

Table 2
Chemical composition of the obtained sodium silicate and sodium aluminate precursors.

Obtained precursor	Concentration (mg/L)									
	Si	Ca	Al	Mg	Fe	Na	Ti	Mn	Zn	Ni
Sodium silicate	8675.87	2.09	1.35	0.04	0.02	31457.82	ND	200.06	10.19	5.46
Sodium aluminate	37.96	1.10	6500.95	ND	0.55	28698.65	20.07	ND	8.26	3.84

Table 3
XRF chemical composition of the as-prepared aluminosilicate.

Oxide/element	SiO_2	CaO	Al_2O_3	MgO	Fe_2O_3	K_2O	Na_2O	P_2O_5	Cl
wt%	55.98	0.95	40.935	0.064	0.64	0.009	0.58	0.012	0.78
Analysis of heavy metals (wt%): Ti = 0.025, Ni = 0.003, Mn = 0.015, Zn = 0.007									

chemical composition. Third, it contributes to the sustainability and economic viability of the industries generating these wastes. Finally, it produces valuable materials, such as aluminosilicate nanopowder, for wastewater treatment, aiding in water recovery and environmental remediation.

This study introduces an environmentally friendly approach for synthesizing mesoporous aluminosilicate powder using two secondary industrial resources: SAD and SMS. The method entails a multistep hydrometallurgy-based conversion process. This sustainable extraction process yielded minimal silica-based insoluble solid residue and holds potential for commercializing inorganic nanocomposites. This research explores the possible application of the synthesized aluminosilicate for adsorbing malachite green (MG) from synthetic dye wastewater.

2. Experimental procedure

2.1. Materials

This study employed two types of industrial waste—SAD and SMS. The granular SAD and SMS clump were sourced from domestic aluminum and ferroalloy production plants, respectively.

Ammonia, sodium hydroxide (NaOH, pellets, 98%), and hydrochloric acid (HCl, 37%) were sourced from a local chemical production company. High-purity sodium chloride (NaCl) and MG chloride dye (a cationic dye, $C_{23}H_{25}ClN_2$) were provided by Merck (Germany). Highly pure ethanol was obtained from Sigma-Aldrich. Deionized water (DI) was utilized to prepare the required solutions.
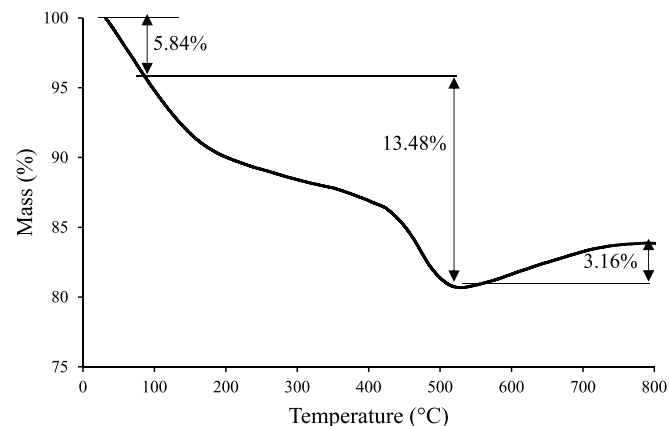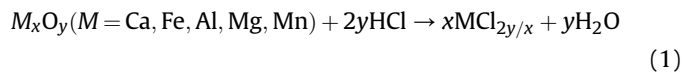

**Fig. 3.** Thermogravimetric analysis of as-prepared aluminosilicate from SAD and SMS.

2.2. Methods

2.2.1. Synthesis process

Fig. 1 displays the flow diagram for the synthesis of aluminosilicate from the SAD and SMS. The synthesis process involved three primary steps: extracting silica from the SMS as a sodium silicate solution (left branch of the synthesis process), extracting alumina from the SAD as a sodium aluminate solution (right branch of the synthesis process), and preparing sodium aluminosilicate powder. As depicted in the left branch of the synthesis process in Fig. 1, the leaching stage was performed using 3 normal HCl (N HCl) at room temperature for 15 min. The liquid-to-solid (acid-to-SMS) ratio was 10 mL/g, achieving a dissolution efficiency of 94%. The potential reactions at this stage are as follows:

$$M_xO_y(M = Ca, Fe, Al, Mg, Mn) + 2yHCl \rightarrow xMCl_{2y/x} + yH_2O \quad (1)$$

$$SiO_2 + 2H_2O \xrightarrow{H^+} Si(OH)_4 \quad (2)$$

The resulting slurry was filtered using Whatman filter paper (No. 41) to separate the acid-insoluble residue from the chloride leachate. After silica extraction, the acid-insoluble residue becomes a rich source of manganese, with manganese content extractable through a suitable hydrometallurgical process. The silicic acid content in the leachate was then converted into a transparent gel by allowing the leachate to age for 24 h in a 1 M NaCl solution. To remove any impurities of metal chloride, the gel was washed several times with a mixture of ethanol and DI (ratio = 3:1). The washed gel was redissolved in the subsequent stage by adding a 2 N NaOH solution (reaction (3)) to obtain the sodium silicate precursor. The potential of hydrogen (pH) value of the sodium silicate precursor achieved was 13.5 ± 0.5.

$$Si(OH)_4 + 2NaOH \rightarrow Na_2SiO_3 + 3H_2O \quad (3)$$
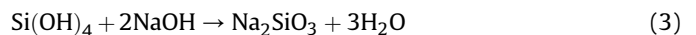
The sodium aluminate precursor was prepared using a previously disclosed method (Mahinroosta & Allahverdi, 2018b). As displayed in the right branch of the synthesis process in Fig. 1, the leaching stage was conducted using 5 N HCl at 85 °C for 2 h. The solid-to-acid ratio was 0.05 g/mL, achieving a dissolution efficiency of 84%. The potential reactions at this stage are as follows:

$$M_xO_y(M = Ca, Fe, Al) + 2yHCl \rightarrow xMCl_{2y/x} + yH_2O \quad (4)$$
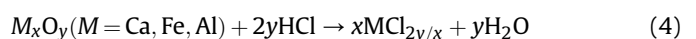
To separate the acid-insoluble residue from the chloride leachate, the resulting slurry was filtered using Whatman filter paper (No. 41). The acid-insoluble residue is a rich source of silica

that is suitable for road construction and concrete applications, as discussed previously in the literature (Mahinroosta & Allahverdi, 2018c; Mahinroosta et al., 2019). In the next stage, a white−yellow precipitate was obtained by adding ammonia (reaction (5)) until the pH reached 10.0 ± 0.5. This precipitate comprises various metal hydroxides.

$$MCl_x(M = Ca, Fe, Al) + xNH_4OH \rightarrow M(OH)_x + xNH_4Cl \quad (5)$$
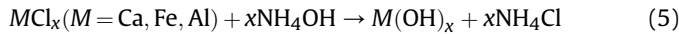
The aluminum hydroxide content of the precipitate was converted into a sodium aluminate precursor by adding 2 N NaOH (reaction (6)), producing a dark brown sol with a pH of 13.5 ± 0.5.

$$Al(OH)_3 + NaOH \rightarrow NaAl(OH)_4 \quad (6)$$

The sol was finally filtered to separate the clear sodium aluminate solution from the mixed metal hydroxides. A mixture of 300 mL of sodium silicate solution and 150 mL of sodium aluminate solution was combined to prepare a precursor for the synthesis of aluminosilicate. The mixture was stirred at 700 rpm for 15 min. The pH value of the sodium aluminosilicate mixture was 13.5 ± 0.5. Adding 3 N HCl until the pH value reached 9.5 ± 0.5 resulted in the appearance of a white precipitate (reaction (7)).

$$NaAl(OH)_4 + Na_2SiO_3 + 3HCl \rightarrow 3NaCl + SiAl(OH)_7 \quad (7)$$
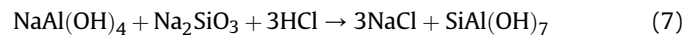
The precipitate was removed from the solution phase through vacuum filtration and washed with DI. The rinsed gel was then oven-dried at 105 °C for 4 h and calcined at 700 °C for 2 h to prepare the aluminosilicate powder. The sodium chloride in the brine produced at the end of the process can be recovered through the solar evaporation system and reused in the process shown in Fig. 1.

2.2.2. Dye removal tests

Tests for removing MG were conducted to evaluate the decolorization efficiency of the synthesized aluminosilicate nanopowder. Appropriate 50 and 100 mg/L MG solutions were prepared for the removal experiments. A typical removal experiment involved stirring 30 mL of the MG solution with 30 mg of adsorbent at 200 rpm. Each dye removal test was performed three times. To calculate the efficiency of dye removal, Equation (1) was used:

$$\%Removal = [(C_0 - C_t) / C_0] \times 100 \quad (8)$$

where C_0 (in mg/L) and C_t (in mg/L) represent the concentrations at times 0 and t, respectively. A Cintra 40 UV-Vis spectrophotometer
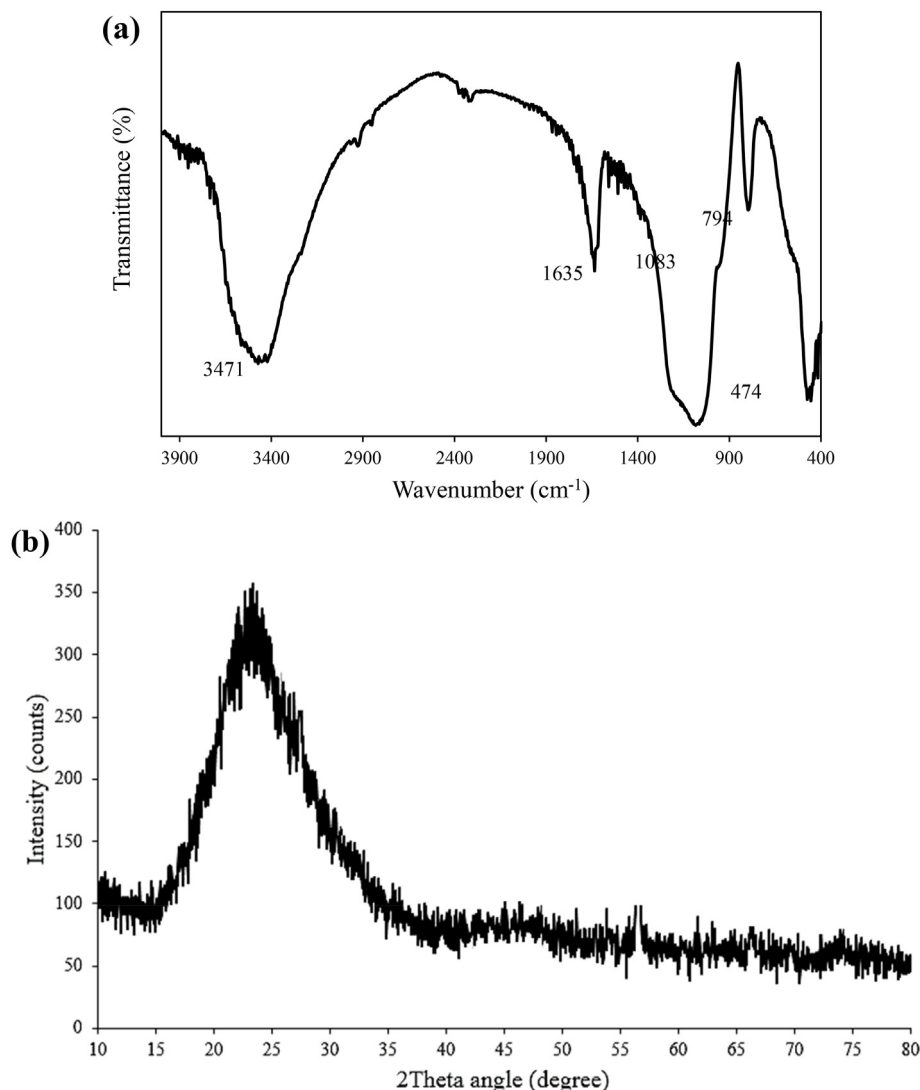

Fig. 4. (a) FTIR spectrum and (b) XRD pattern of as-synthesized aluminosilicate powder.

was used to measure the concentration of the MG solution after the removal test at 625 nm.

2.2.3. Characterization analyses

The X-ray diffraction (XRD) patterns of the industrial wastes and the prepared aluminosilicate were obtained using a Dutch Philips diffractometer (PW1730 X-ray) within a 2θ range of 5°−80°. The chemical analysis of the starting materials and the synthesized aluminosilicate was performed using an X-ray fluorescence device (Philips PW1410, Netherlands). Chemical bonds were analyzed using a Japanese Fourier transform infrared (FTIR) spectrometer (SHIMADZU 8400 s) in the 400−4000 cm^{-1} range, with the FTIR data gathered in transmittance mode. Field emission scanning electron microscopy (FESEM) (TESCAN MIRA III, Czech Republic, 15 kV) and high-resolution transmission electron microscopy (HRTEM) (FEI Titan 80−300, 300 kV) were used to examine the synthesized aluminosilicate microstructure. A BELSORP MINI II (Japan) sorptometer was employed to obtain the N_2 adsorption—desorption data of the aluminosilicate at 77 K. The particle size distribution of the prepared aluminosilicate was determined using dynamic light scattering (DLS) with a Scatteroscope I device (South Korea). Thermogravimetry data of the aluminosilicate were obtained using an SDT Q600 thermoanalyzer (USA) under an air atmosphere with a heating rate of 10 °C/min. The chemical composition of the prepared precursors was determined using inductively coupled plasma atomic emission spectroscopy (ICP-AES) with PerkinElmer Optima 7300 D equipment (USA).

3. Results and discussion

3.1. Characterization of industrial wastes

The as-received SMS and SAD exhibited light green−gray and gray colors, respectively. The SMS was crushed into pieces smaller than 5 mm. Detailed compositions of the SMS and SAD can be referenced in Table 1.

Following the data in Table 1, the SAD is rich in aluminum oxide. The SMS chemical composition indicates that the primary constituents are silica, calcium oxide, aluminum oxide, and manganese dioxide. The loss on ignition value measured at 950 ± 50 °C for the SAD and SMS was 14.12 and 1.4 wt%, respectively. Fig. 2 shows the XRD mineralogy of the SAD and SMS. The SAD XRD pattern reveals corundum (ICDD-01-078-1254), $MgAl_2O_4$ spinel (ICDD-01-087-0344), diaoyudaoite ($NaAl_{11}O_{17}$) (ICDD-01-072-0587), cryolite (Na_3AlF_6) (COD-96-901-2285), and aluminum nitride (AlN) (icdd-01-070-0779) as the sources of aluminum. The SMS XRD pattern shows gehlenite ($Ca_2Al_2SiO_7$) (COD- 96-900-6113), glaucochroite ($[Ca, Mn]_2SiO_7$) (ICDD 14-376), and quartz (SiO_2) (COD-96-901-3322) as the primary crystalline phases. Earlier studies
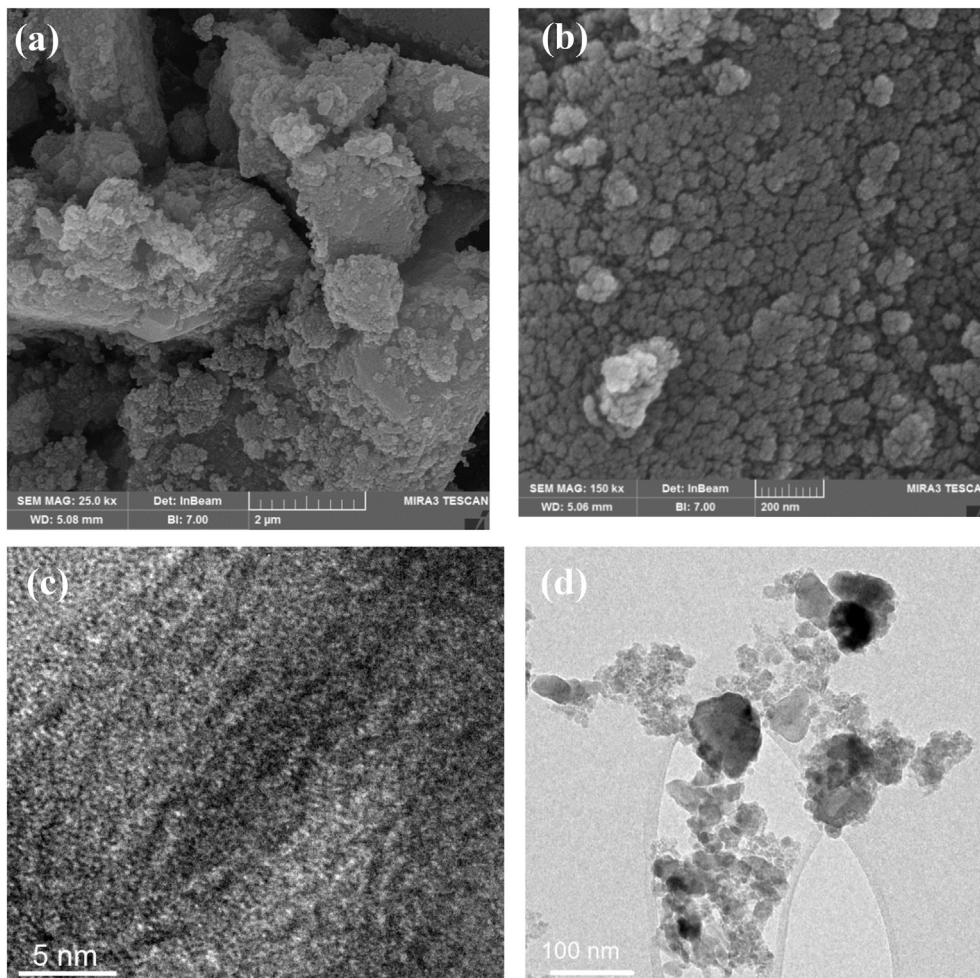

Fig. 5. (a, b) FESEM and (c, d) HRTEM micrographs of as-prepared aluminosilicate from secondary aluminum dross and silicomanganese slag.

documented similar phases (Mahinroosta and Allahverdi, 2020, 2021; Mohammadzadeh et al., 2022).

3.2. Composition analysis of the obtained precursors

Table 2 presents the chemical analysis of the sodium silicate and sodium aluminate precursors, as determined using the ICP-AES technique. As depicted in Fig. 1, sodium silicate and aluminate are the primary products obtained from extracting silica from SMS and alumina from SAD, respectively.

As shown in Table 2, the sodium silicate precursor exhibited a high purity of silicon (Si), while the sodium aluminate precursor demonstrated a high purity of aluminum (Al). The high sodium content in both precursors can be attributed to the use of aqueous NaOH during the redissolution stage. Trace amounts of silica in the chemical composition of the sodium aluminate precursor are likely due to the partial dissolution of the silica content in the SAD under alkaline conditions. Table 3 presents the X-ray fluorescence (XRF) chemical composition of the as-prepared aluminosilicate. The combined SiO_2 and Al_2O_3 content accounts for approximately 97 wt% of the total material composition. The total heavy metal content in the chemical composition of the synthesized aluminosilicate was approximately 0.05 wt%. This negligible amount poses no significant concern regarding using the synthesized aluminosilicate as an adsorbent for wastewater treatment applications.

The presence of CaO and MnO primarily originates from the initial SMS, while the minimal Fe_2O_3 impurity is attributed to the SAD composition. The existence of Na_2O is likely linked to NaOH utilization during the synthesis process. The synthesized aluminosilicate contains 55.98 g of SiO_2 and 40.935 g of Al_2O_3 per 100 g of the material, based on the mass fractions presented in Table 3. Considering the molar masses of SiO_2 (60.08 g/mol) and Al_2O_3 (101.96 g/mol), their respective molar fractions are 0.932 and 0.401,

indicating that the chemical formula of the aluminosilicate can be expressed as $[Al_2O_3]_{(0.401)} \cdot [SiO_2]_{(0.932)}$ or $Al_2O_3 \cdot 2.3SiO_2$.

3.3. Thermogravimetric analysis

The thermogravimetric analysis curve of the as-prepared aluminosilicate powder is shown in Fig. 3. The curve was plotted based on data recorded in the temperature range of 25−800 °C. A mass loss of approximately 5.9% at 100 °C corresponds to the evaporation of adsorbed moisture. The mass loss of approximately 13.5% between 100 and 527 °C is attributed to the elimination of hydroxyl water from the hydrogel structure, forming the Si−O−Al bond. The 3% increase in mass is due to the readsorption of water on the material's surface, occurring as water separates from the aluminosilicate structure and forms a fine microstructure. These findings are significant because the Si−O−Al bonds, which constitute the primary bonds in the aluminosilicate structure, remain intact over various temperatures. This suggests that the conditions are favorable for utilizing the adsorbent in high-temperature effluents or for the thermal regeneration of the spent adsorbent.

3.4. Determination of chemical bonds and crystalline structure

Fig. 4 displays the FTIR spectrum and XRD pattern of the synthesized aluminosilicate powder. The absorption bands at 474 and 1083 cm^{-1} are associated with Si−O and −Si−OH bending vibrations, respectively (Frost et al., 1996). The absorption band at 794 cm^{-1} corresponds to the stretching vibration of Si−O−Al (Jara et al., 2005). The presence of an oxo-bridge suggests the formation of aluminosilicate bonds. The bands at 1635 and 3471 cm^{-1} correspond to the stretching vibration of the O−H bond (Pereira et al., 2019).

The XRD pattern in Fig. 4 reveals a hump at a 2θ angle of approximately 23°, indicating the amorphous nature of the
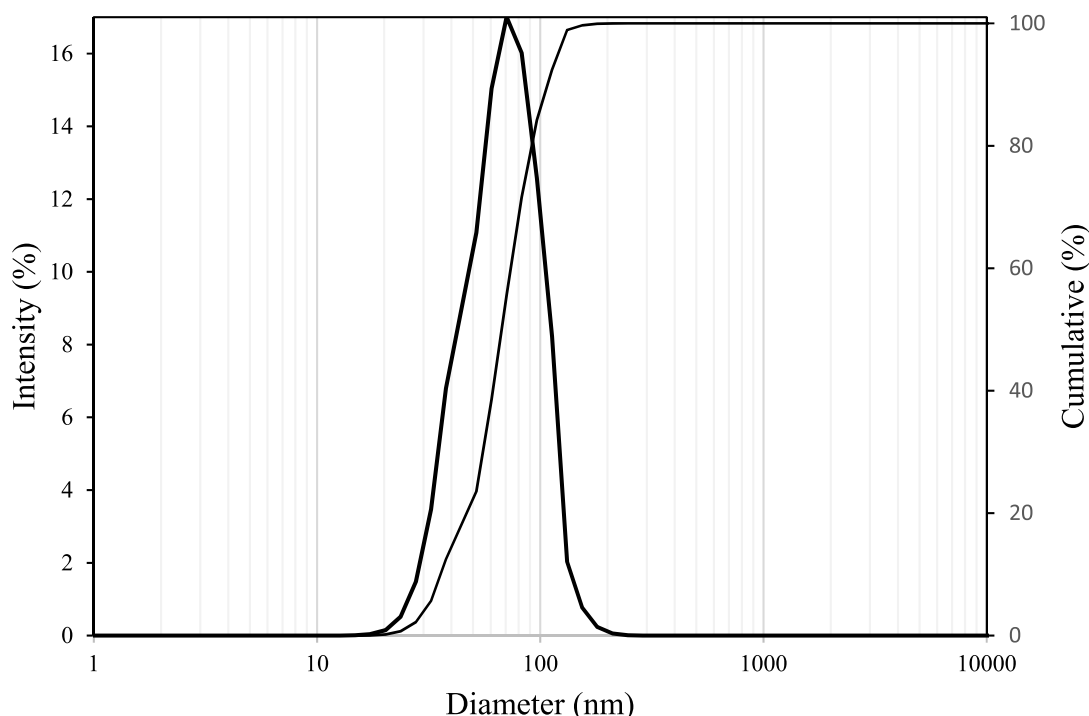

Fig. 6. Particle size distribution of as-synthesized aluminosilicate nanoparticles.

synthesized aluminosilicate. Similar amorphous peaks have been reported in previous studies by Zheng et al. (2012), Pereira et al. (2019), and Diwakar et al. (2018). Additionally, another amorphous hump was detected at a 2θ angle of approximately 2° by small-angle XRD. Research has demonstrated that aluminosilicate with a Si:Al molar ratio of approximately 1 (Si:Al = 1.16 in this study) exhibits an amorphous structure (Shalygin et al., 2017).

3.5. Microstructural analysis

Fig. 5 illustrates the FESEM and HRTEM micrographs of the synthesized aluminosilicate powder. Fig. 5(a) shows a disordered clump structure with numerous particle agglomerates. Fig. 5(b) further reveals that these agglomerates comprised nanoparticles. Nanomaterials tend to agglomerate due to their high surface energy, especially at elevated mineral contents (Muthu & Santhanam, 2018; Tavandashti et al., 2009; Tyson et al., 2011).

Fig. 5(c) and (d) show the synthesized aluminosilicate HRTEM micrographs. The absence of an ordered microstructure in Fig. 5(c) indicates that the synthesized aluminosilicate is entirely amorphous. This result agrees with the XRD pattern (Fig. 4). Fig. 5(d) displays

particles ranging in size from 20 to 80 nm, contributing to the formation of the large agglomerates from 1 to 5 μm depicted in Fig. 5(a).

3.6. Particle size distribution

The particle size distribution results of the aluminosilicate nanoparticles are presented in Fig. 6. The D_{50}, representing the average particle size, indicates that 50% of the aluminosilicate nanoparticles are larger than 70.7 nm, while the other 50% are smaller than this value. Similarly, the D_{90} and D_{10} represent the particle sizes below which 90% and 10% of the scattering particles fall, respectively. The D_{90} and D_{10} correspond to particle sizes of 94.87 and 24.49 nm, respectively. Comparing the particle size distribution results from the DLS analysis with those from the microscopic analyses may not be entirely logical. The DLS analysis measures the hydrodynamic diameter of particles using light diffraction, whereas microscopic techniques, such as TEM, measure particle size based on electron passage through the material. However, in this study, the proximity of the DLS results to the particle sizes from microscopic analysis suggests the presence of numerous individual particles.
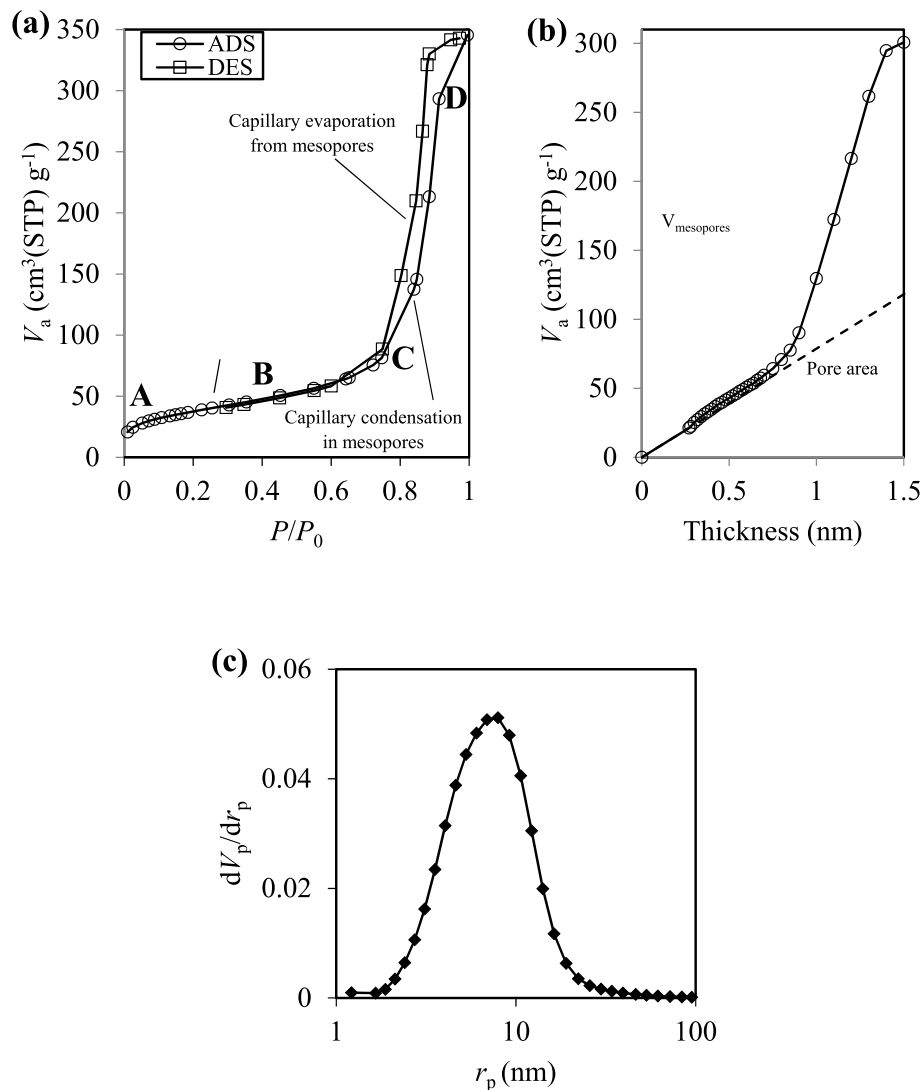

Fig. 7. (a) Nitrogen adsorption-desorption of the as-synthesized aluminosilicate; (b) t-plot method for calculation of pore area and volume of mesopores; (c) pore size distribution of the as-synthesized aluminosilicate.

3.7. Surface and porosimetry studies

Fig. 7(a) displays the nitrogen sorption data of the prepared aluminosilicate. According to the International Union of Pure and Applied Chemistry (IUPAC) classification of adsorption isotherms, the prepared aluminosilicate exhibited a type IV isotherm, concave to the P/P_0 axis, characteristic of mesoporous materials. The t-plot method is dependable for analyzing the nitrogen sorption data of porous materials. In this method, the relative pressure data are converted to the thickness of the adsorbate using the Harkins and Jura equation (Harkins & Jura, 1944).

$$t = (13.99/(0.034 - \log_{10}(P/P_0)))^{0.5} \tag{9}$$

Fig. 7(b) illustrates the t-plot obtained for the prepared aluminosilicate. A mesoporous material typically displays a t-plot with two distinct regimes. Initially, at low thicknesses/pressures, adsorption occurs within the mesopores. Once the mesopores reach saturation, adsorption shifts to the external surface of the mesoporous particles, leading to a broader range of thickness/pressure. In Fig. 7(a), the adsorption branch is segmented into regions A, B, C, and D. Region A signifies the monolayer adsorption of nitrogen molecules on the pore walls. Region B corresponds to the multilayer adsorption of N_2. Regions C to D indicate capillary condensation within the mesopores. The total specific surface area was calculated by multiplying the slope of this line by 1.55 (Galarneau et al., 2014), resulting in a value of 122.08 m^2/g. The volume of mesopores was 47 cm^3/g, calculated by multiplying 0.00155 by the volume indicated by the dashed line. The micropore volume was obtained by subtracting the mesopore volume from the total volume ($V_{micropores} = V_{total} - V_{mesopores}$).

The pore size distribution depicted in Fig. 7(c) reveals an average pore diameter of approximately 15.8 nm, confirming the mesoporosity of the obtained materials following IUPAC classification.

3.8. Removal of MG dye

Fig. 8 illustrates the efficiency of MG dye removal and the adsorption amount from 5 to 90 min. Removal efficiencies ranging
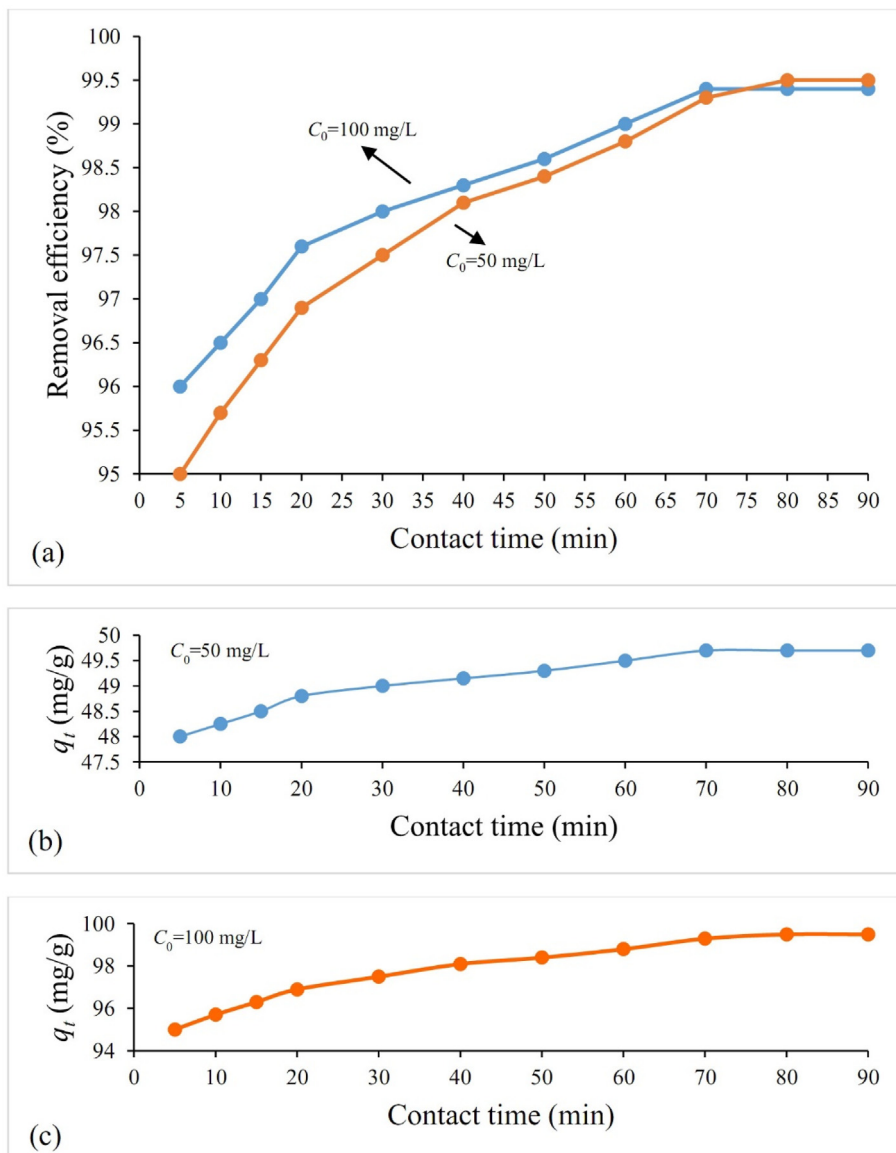

Fig. 8. (a) Malachite green removal efficiency and (b,c) adsorption amount against contact time, adsorbent dosage = 1 g/L (standard deviation < 2.8%).
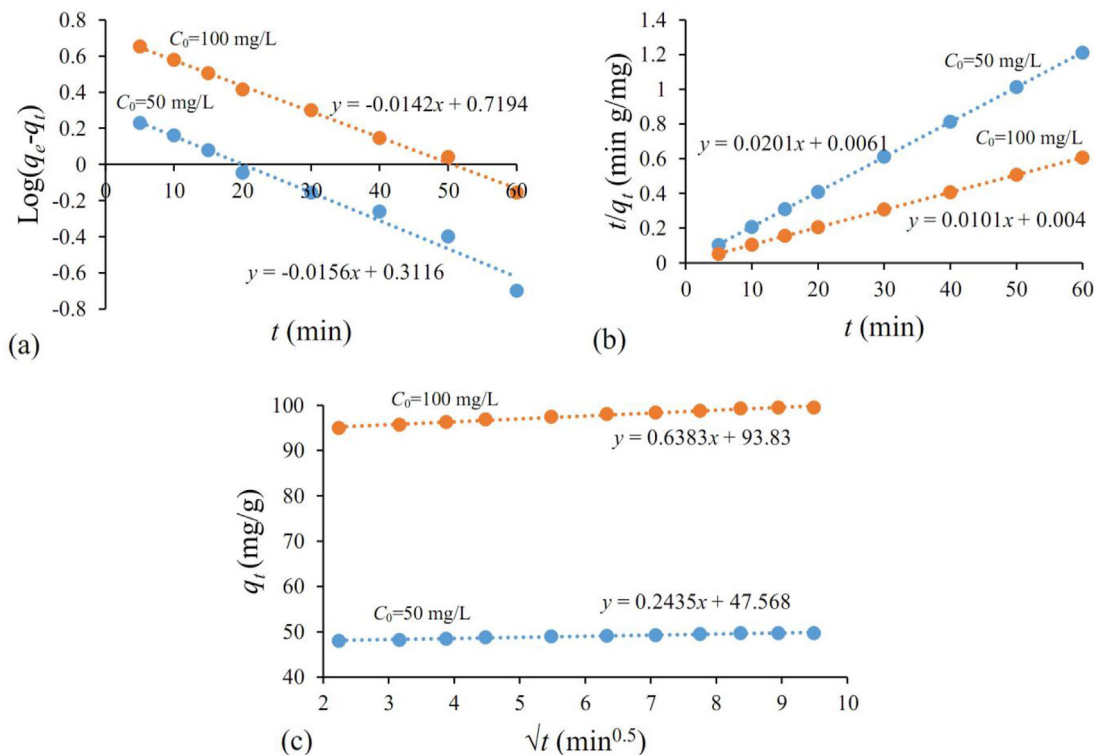
Fig. 9. Kinetic studies of MG adsorption by aluminosilicate nanopowder in (Standard deviation <4.4%); (a) pseudo-first order model, (b) pseudo-second order model, and(c) intraparticle diffusion model.

from 96.3% to 97.0% were achieved after 15 min. The kinetics curve suggests a two-step process for MG dye removal, with rapid initial removal followed by a slower phase until reaching a constant value. By the 80-min mark, approximately 99.5% of the MG dye can be removed from the aqueous solution. The data in Fig. 8 also indicate that MG uptake increases with longer contact times and higher initial MG concentrations. Initially, the rate of MG uptake is rapid but gradually slows down until equilibrium is reached. For an initial MG concentration of 50 mg/L, increasing the duration from 5 to 70 min resulted in MG uptake increasing from 48 to 49.7 mg/g. Further extension of contact time did not significantly impact MG adsorption. For an initial MG concentration of 100 mg/L, MG uptake increased from 95 to 99.5 mg/g as the duration increased from 5 to 80 min. Beyond this point, the MG uptake remained stable. The equilibrium contact time for both initial MG concentrations was 80 min based on the results.

The pseudo-first-order, pseudo-second-order, and intraparticle diffusion kinetics models were utilized to analyze the kinetics of MG adsorption on an aluminosilicate nanopowder adsorbent. Fig. 9 illustrates the fits of the experimental data for MG adsorption by aluminosilicate nanopowder using these kinetic models. All three models exhibit high correlation coefficients (R^2), as depicted in Fig. 9. The χ^2 nonlinear statistic was employed to determine the

most suitable model. Table 4 displays the values of R^2, χ^2, and the kinetic constants for all three models.

Based on the R^2 and χ^2 values, the experimental data for MG adsorption by the aluminosilicate nanopowder aligned with the intraparticle diffusion kinetic model. A nonzero and positive y-intercept suggests that MG adsorption by the adsorbent involves rapid adsorption and diffusion mechanisms. The adsorption isotherms were analyzed using the Freundlich and Langmuir models. The Freundlich model, an empirical equation, assumes adsorption on heterogeneous surfaces. However, the Langmuir model describes monolayer adsorption on surfaces with sites of uniform energy without interactions between adsorbate molecules. The linearized forms of the Freundlich and Langmuir models are as follows:

$$\log q_e = \log K_f + (1/n)\log C_e \tag{10}$$

$$C_e/q_e = 1/q_{\max}b + C_e/q_{\max} \tag{11}$$

where n and K_f are two important constants indicating adsorption desirability and capacity, respectively. The parameter $q_{\max}$ denotes the maximum adsorption capacity, and the adsorption energy can be inferred from the constant b. Additionally, the separation

Table 4
Constants of kinetic models of adsorption of MG by aluminosilicate nanopowder.

| Model	Pseudo-first order kinetic model				Pseudo-second order kinetic model				Intraparticle diffusion kinetic model			
Formula	$\log(q_e - q_t) = \log q_e - (k_{ad}/2.303)t$				$t/q_t = (1/kq_e^2) + (1/q_e)t$				$q_t = K_n t^{1/2} + C_n$			
Parameter	R^2	χ^2	k_{ad} (min^{-1})	q_e (mg/g)	R^2	χ^2	k (g/mg min)	q_e (mg/g)	R^2	χ^2	K_n (mg/min$^{1/2}$g)	C_n (mg/g)
Value (50 mg/L)[a]	0.97	1.03	0.037	2.05	0.99	0.046	0.025	100	0.98	0.0003	0.24	47.57
Value (100 mg/L)[a]	0.99	2.73	0.033	5.25	0.99	0.027	0.065	50	0.97	0.0007	0.64	93.83

[a] Initial MG concentration.
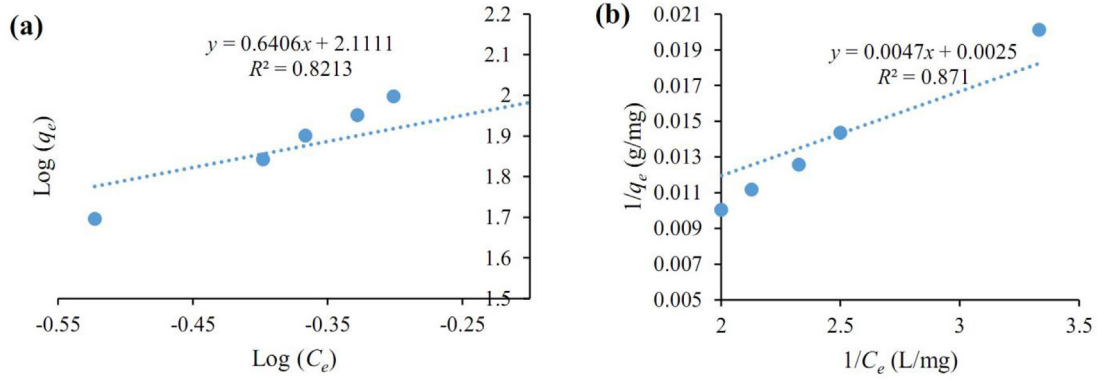
Fig. 10. Adsorption isotherms for adsorption of MG by the aluminosilicate nanopowder, (a) Freundlich and (b) Langmuir (Standard deviation <4.6%).
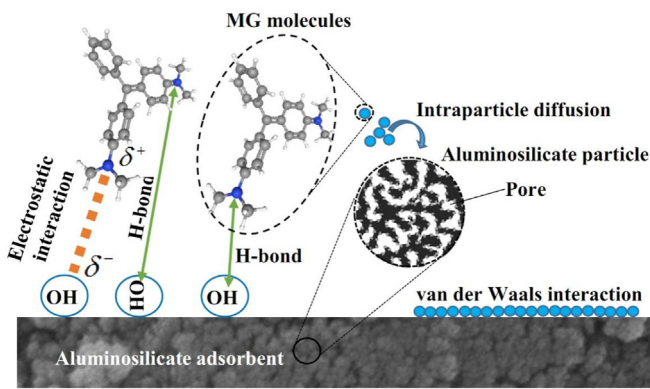

Fig. 11. Potential mechanisms for the removal of MG dye by the synthesized aluminosilicate adsorbent.

coefficient, R_L, of the Langmuir model determines the favorability of the adsorption process.

$$R_{\mathrm{L}} = 1 / (1 + bC_0) \tag{12}$$

The values of $R_{\mathrm{L}} > 1$ and $R_{\mathrm{L}} = 0$ indicate undesirable and irreversible adsorption, respectively. However, the range of $0 < R_{\mathrm{L}} < 1$ suggests desirable adsorption. Fig. 10 shows the fitting of the Freundlich and Langmuir isotherms to the equilibrium adsorption data of MG by the aluminosilicate nanopowder. These data were obtained under conditions with a contact time of 80 min and an adsorbent dosage of 1 g/L. The Langmuir parameters of q_{max} and b are 400 mg/g and 0.53 L/mg, respectively. The values of the separation factor, R_{L}, for all initial concentrations of the MG solution are less than 1, indicating favorable adsorption of MG by the synthesized aluminosilicate adsorbent. The Freundlich parameters K_f and n are 128.82 (mg/g) (L/mg)$^{0.64}$ and 1.56, respectively. The value of n between 1 and 10 confirms the favorable MG adsorption. The higher R^2 correlation coefficients suggest that the Freundlich isotherm better predicts the adsorption data, implying that chemisorption is the primary mechanism for MG dye adsorption.

As illustrated in Fig. 11, the MG molecules are adsorbed onto the high surface area of the aluminosilicate adsorbent through van der Waals forces and electrostatic interactions. The mesoporous structure of the aluminosilicate allows MG molecules to penetrate the pores, enhancing adsorption capacity. Functional groups on the aluminosilicate surface, such as silanol (Si−OH) and aluminol (Al−OH), facilitate MG chemisorption through hydrogen bonding and electrostatic attraction mechanisms. Intraparticle diffusion of MG into the aluminosilicate pores is a crucial step in the overall adsorption process, as evidenced by the nonzero intercept in the intraparticle diffusion model (Hussien Hamad, 2023).
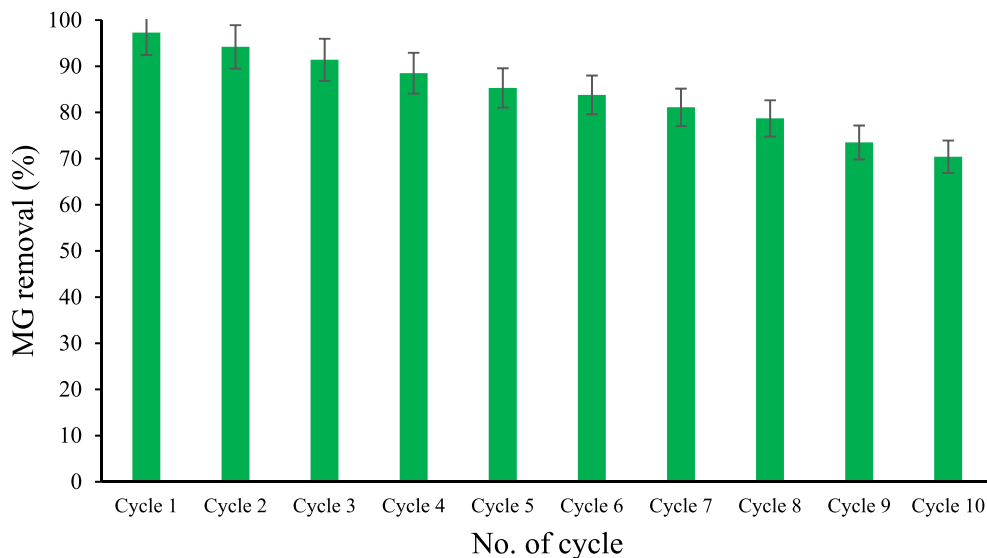

Fig. 12. MG dye removal percentage in different cycles of adsorption process.

Table 5

A comparison of the maximum adsorption capacities based on Langmuir model for MG dye among various adsorbents.

Adsorbent	Maximum capacity (mg/g)	Ref.
Aluminosilicate nanopowder from aluminum dross and silicomanganese slag	400.0	This study
Rumex abyssinicus-derived activated carbon	98.4	Abewaa et al. (2023)
Pakistani bentonite clay	243.9	Ullah et al. (2021)
Turkish red mud	172.4	
Extracellular polymeric substance of Lysinibacillus sp. SS1	178.6	Kamath Miyar et al., 2021
Activated carbon of *Catha* edulis stem	5.6	Abate et al. (2020)
Mesoporous chitosan−zinc oxide composite	11.0	Muinde et al. (2020)
Wood apple shells	35.8	Sartape et al. (2017)
Acid-activated carbon	32.8	Piriya et al. (2023)
Biosilica	40.7	Dubey et al. (2024)
Modified bagasse fly ash	18.7	Gebre Meskel et al., 2024

Fig. 12 illustrates the percentage of MG dye removal across various cycles of the adsorption process. The tests were conducted with an adsorbent dose of 1 g/L and an adsorption time of 80 min. Before each cycle, the spent adsorbent underwent leaching using 1 N HCl at 45 °C for 1 h and was washed with water at 95 °C for an additional hour. Subsequently, the adsorbent was oven-dried at 110 °C. The data in Fig. 12 indicate that the adsorbent achieved over 90% MG dye removal after three cycles. However, in the fourth to seventh cycles, the efficiency decreased below 90%, and beyond the eighth cycle, it dropped below 80%. These findings demonstrate the favorable reusability of the aluminosilicate adsorbent derived from the two industrial wastes.

Table 5 compares the maximum adsorption capacities for MG dye among various adsorbents. As evident from Table 5, the aluminosilicate adsorbent synthesized from the SAD and SMS in this study exhibits a significantly higher adsorption capacity than the other adsorbents. In addition to adsorption capacity, considering the optimal conditions for utilizing these adsorbents in removing MG dye is crucial. These optimal conditions encompass factors such as pH, adsorbent dosage, adsorption duration, and interfering ions.

4. Conclusions

This study demonstrated the preparation of mesoporous aluminosilicate nanopowder from SMS and SAD. The SAD alumina content and SMS silica content were extracted as sodium aluminate and sodium silicate, respectively, through a hydrometallurgical process. The preparation route involved acid leaching, precipitation, aging, redissolution, and calcination stages. Acid leaching was conducted using aqueous HCl under atmospheric pressure. Ammonia and aqueous NaOH were used as precipitants and redissolving agents, respectively. The proposed process can treat over 84% of SMS and SAD. Characterization analyses revealed that the prepared aluminosilicate exhibits a mesoporous amorphous structure with a relatively high specific surface area of 122.08 m^2/g, average pore size of 15.8 nm, particle size of 20−80 nm, and high purity of about 97 wt%, making it suitable for catalytic and adsorption applications. Based on MG dye removal experiments, the aluminosilicate nanopowder can remove 99.5% of the dye within 80 min. The kinetic model fitting of the aluminosilicate adsorbent indicated that the intraparticle diffusion model best predicts the adsorption data. Analysis of adsorption isotherm models also suggested that the Freundlich model can fit the equilibrium adsorption data, implying the chemisorption of the dye on the adsorbent surface. The Langmuir isotherm model yielded a maximum dye adsorption capacity of 400 mg/g, paralleling the results reported in the literature.

Disclosure instructions

During the preparation of this study, the author(s) used [Wordvice AI] to improve readability and language. After using this tool/service, the author(s) reviewed and edited the content as needed and take(s) full responsibility for the content of the publication.

CRediT authorship contribution statement

Mostafa Mahinroosta: Writing − review & editing, Writing − original draft, Visualization, Validation, Supervision, Software, Resources, Project administration, Methodology, Investigation, Formal analysis, Data curation, Conceptualization. **Rozita M. Moattari:** Writing − original draft, Validation, Software, Methodology, Investigation, Formal analysis. **Ali Allahverdi:** Supervision, Resources, Methodology, Funding acquisition. **Pooria Ghadir:** Writing − original draft, Resources, Methodology, Investigation, Formal analysis, Data curation.

Declaration of competing interest

The authors declare no conflicts of interest.

References

Abate, G. Y., Alene, A. N., Habte, A. T., & Getahun, D. M. (2020). Adsorptive removal of malachite green dye from aqueous solution onto activated carbon of Catha edulis stem as a low cost bio-adsorbent. *Environmental Systems Research, 9*, 29. https://doi.org/10.1186/s40068-020-00191-4

Abewaa, M., Mengistu, A., Takele, T., Fito, J., & Nkambule, T. (2023). Adsorptive removal of malachite green dye from aqueous solution using Rumex abyssinicus derived activated carbon. *Scientific Reports, 13*, Article 14701. https://doi.org/10.1038/s41598-023-41957-x

Akhlaghian, F., Ghadermazi, M., & Chenarani, B. (2014). Removal of phenolic compounds by adsorption on nano structured aluminosilicates. *Journal of Environmental Chemical Engineering, 2*, 543−549. https://doi.org/10.1016/j.jece.2013.10.009

Choi, S., Kim, J., Oh, S., & Han, D. (2017). Hydro-thermal reaction according to the CaO/SiO$_2$ mole-ratio in silico-manganese slag. *Journal of Material Cycles and Waste Management, 19*, 374−381. https://doi.org/10.1007/s10163-015-0431-6

Diwakar, J., Viswanadham, N., Saxena, S. K., Kumar, S., & Al-Muhtaseb, A. H. (2018). Liquid-phase solvent-less reactions for value addition of glycerol and phenols over nano porous aluminosilicates. *Materials Today Communications, 15*, 260−268. https://doi.org/10.1016/j.mtcomm.2018.03.014

Duan, C., Cao, Y., Hu, L., Zhang, Y., Fu, D., Ma, J., & Zhang, J. (2019). Mechanochemical synthesis of the α-AlH$_3$/LiCl nano-composites by reaction of LiH and AlCl$_3$: Kinetics modeling and reaction mechanism. *International Journal of Hydrogen Energy, 44*, 23716−23725. https://doi.org/10.1016/j.ijhydene.2019.07.092

Dubey, S., Mishra, R. K., Kaya, S., Rene, E. R., Giri, B. S., & Sharma, Y. C. (2024). Microalgae derived honeycomb structured mesoporous diatom biosilica for adsorption of malachite green: Process optimization and modeling. *Chemosphere, 355*, Article 141696. https://doi.org/10.1016/j.chemosphere.2024.141696

Fotukian, S. M., Barati, A., Soleymani, M., & Alizadeh, A. M. (2020). Solvothermal synthesis of CuFe$_2$O$_4$ and Fe$_3$O$_4$ nanoparticles with high heating efficiency for

magnetic hyperthermia application. *Journal of Alloys and Compounds, 816*, Article 152548. https://doi.org/10.1016/j.jallcom.2019.152548

Frías, M., de Rojas, M. I. S., & Rodríguez, C. (2009). The influence of SiMn slag on chemical resistance of blended cement pastes. *Construction and Building Materials, 23*, 1472–1475.

Frost, R. L., Frederick, P. M., & Shurvell, H. F. (1996). Raman microscopy of some kaolinite clay minerals. *Canadian journal of applied spectroscopy, 41*, 10–14.

Fu, Z., Liu, T., Kong, X., Liu, Y., Xu, J., Zhang, B., Chen, H., & Chen, Z. (2019). Synthesis and characterization of nano-layered Mg-vermiculite by hydrothermal method. *Materials Letters, 238*, 175–178. https://doi.org/10.1016/j.matlet.2018.11.148

Galarneau, A., Villemot, F., Rodriguez, J., Fajula, F., & Coasne, B. (2014). Validity of the *t*-plot method to assess microporosity in hierarchical micro/mesoporous materials. *Langmuir, 30*, 13266–13274. https://doi.org/10.1021/la5026679

Gebre Meskel, A., Kwikima, M. M., Meshesha, B. T., Habtu, N. G., Naik, S. V. C. S., & Vellanki, B. P. (2024). Malachite green and methylene blue dye removal using modified bagasse fly ash: Adsorption optimization studies. *Environmental Challenges, 14*, Article 100829. https://doi.org/10.1016/j.envc.2023.100829

Harkins, W. D., & Jura, G. (1944). Surfaces of solids. XII. An absolute method for the determination of the area of a finely divided crystalline solid. *Journal of the American Chemical Society, 66*, 1362–1366. https://doi.org/10.1021/ja01236a047

Hussien Hamad, M. T. M. (2023). Optimization study of the adsorption of malachite green removal by MgO nano-composite, nano-bentonite and fungal immobilization on active carbon using response surface methodology and kinetic study. *Environmental Sciences Europe, 35*, 26. https://doi.org/10.1186/s12302-023-00728-1

Jara, A. A., Goldberg, S., & Mora, M. L. (2005). Studies of the surface charge of amorphous aluminosilicates using surface complexation models. *Journal of Colloid and Interface Science, 292*, 160–170. https://doi.org/10.1016/j.jcis.2005.05.083

Kamath Miyar, H., Pai, A., & Goveas, L. C. (2021). Adsorption of malachite green by extracellular polymeric substance of *Lysinibacillus* sp. SS1: Kinetics and isotherms. *Heliyon, 7*, Article e07169. https://doi.org/10.1016/j.heliyon.2021.e07169

Kant Sharma, R., Gautam, P., Kumar, A., & Mandal, K. D. (2017). Synthesis of sphere-like nano-crystalline Co_3O_4 spinel via a simple homogeneous precipitation method. *Materials Today: Proceedings, 4*, 5667–5671. https://doi.org/10.1016/j.matpr.2017.06.028

Kim, B. S., Jeong, S. B., Jeong, M. H., & Ryu, J. W. (2011). Upgrading of manganese from waste silicomanganese slag by a mechanical separation process. *Materials Transactions, 52*, 1705–1708. https://doi.org/10.2320/matertrans.M2011114

Kumar, S., García-Triñanes, P., Teixeira-Pinto, A., & Bao, M. (2013). Development of alkali activated cement from mechanically activated silico-manganese (SiMn) slag. *Cement and Concrete Composites, 40*, 7–13. https://doi.org/10.1016/j.cemconcomp.2013.03.026

Leidich, S., Buechele, D., Lauenstein, R., Kluenker, M., & Lind, C. (2016). "Non-hydrolytic" sol–gel synthesis of molybdenum sulfides. *Journal of Solid State Chemistry, 242*, 175–181. https://doi.org/10.1016/j.jssc.2016.02.020

Liu, W., Liu, X., Zhang, P., Wang, Z., Li, X., & Hu, M. (2019). Nano-sized plate-like alumina synthesis via solution combustion. *Ceramics International, 45*, 9919–9925.

Lopes, A. C., Martins, P., & Lanceros-Mendez, S. (2014). Aluminosilicate and aluminosilicate based polymer composites: Present status, applications and future trends. *Progress in Surface Science, 89*, 239–277. https://doi.org/10.1016/j.progsurf.2014.08.002

Mahinroosta, M., & Allahverdi, A. (2018a). Hazardous aluminum dross characterization and recycling strategies: A critical review. *Journal of Environmental Management, 223*, 452–468. https://doi.org/10.1016/j.jenvman.2018.06.068

Mahinroosta, M., & Allahverdi, A. (2018b). Enhanced alumina recovery from secondary aluminum dross for high purity nanostructured γ-alumina powder production: Kinetic study. *Journal of Environmental Management, 212*, 278–291. https://doi.org/10.1016/j.jenvman.2018.02.009

Mahinroosta, M., & Allahverdi, A. (2018c). A promising green process for synthesis of high purity activated-alumina nanopowder from secondary aluminum dross. *Journal of Cleaner Production, 179*, 93–102. https://doi.org/10.1016/j.jclepro.2018.01.079

Mahinroosta, M., & Allahverdi, A. (2020). Production of high purity α- and γ-alumina from aluminum dross. In S. Hashmi, & I. A. Choudhury (Eds.), *Encyclopedia of renewable and sustainable materials*. Amsterdam: Elsevier.

Mahinroosta, M., & Allahverdi, A. (2021). Pilot-scale valorization of hazardous aluminum dross into γ-Al_2O_3 nanoadsorbent for efficient removal of fluoride. *Environmental Technology & Innovation, 23*, Article 101549. https://doi.org/10.1016/j.eti.2021.101549

Mahinroosta, M., Allahverdi, A., Dong, P., & Bassim, N. (2019). Green template-free synthesis and characterization of mesoporous alumina as a high value-added product in aluminum black dross recycling strategy. *Journal of Alloys and Compounds, 792*, 161–169. https://doi.org/10.1016/j.jallcom.2019.04.009

Meng, L., & Zhao, H. (2020). Low-temperature complete removal of toluene over highly active nanoparticles CuO-TiO_2 synthesized via flame spray pyrolysis. *Applied Catalysis B: Environmental, 264*, Article 118427. https://doi.org/10.1016/j.apcatb.2019.118427

Mohammadzadeh, K., Mahinroosta, M., Allahverdi, A., Dong, P., & Bassim, N. (2022). Non-supercritical drying synthesis and characterization of monolithic alumina aerogel from secondary aluminum dross. *Ceramics International, 48*, 13154–13162. https://doi.org/10.1016/j.ceramint.2022.01.192

Muinde, V. M., Onyari, J. M., Wamalwa, B., & Wabomba, J. N. (2020). Adsorption of malachite green dye from aqueous solutions using mesoporous chitosan–zinc oxide composite material. *Environmental Chemistry and Ecotoxicology, 2*, 115–125. https://doi.org/10.1016/j.enceco.2020.07.005

Muthu, M., & Santhanam, M. (2018). Effect of reduced graphene oxide, alumina and silica nanoparticles on the deterioration characteristics of Portland cement paste exposed to acidic environment. *Cement and Concrete Composites, 91*, 118–137. https://doi.org/10.1016/j.cemconcomp.2018.05.005

Naderi-Beni, B., & Alizadeh, A. (2020). Development of a new sol-gel route for the preparation of aluminum oxynitride nano-powders. *Ceramics International, 46*, 913–920. https://doi.org/10.1016/j.ceramint.2019.09.049

Najamuddin, S. K., Johari, M. A. M., Maslehuddin, M., & Yusuf, M. O. (2019). Synthesis of low temperature cured alkaline activated silicomanganese fume mortar. *Construction and Building Materials, 200*, 387–397.

Namvar, M., Mahinroosta, M., & Allahverdi, A. (2021). Highly efficient green synthesis of highly pure microporous nanosilica from silicomanganese slag. *Ceramics International, 47*, 2222–2229. https://doi.org/10.1016/j.ceramint.2020.09.062

Namvar, M., Mahinroosta, M., & Allahverdi, A. (2023). Valorization of silicomanganese slag into reusable porous high-performance nanosilica for recovery of water from methylene blue wastewater. *Journal of Sustainable Metallurgy, 9*, 132–147. https://doi.org/10.1007/s40831-022-00634-5

Namvar, M., Mahinroosta, M., Allahverdi, A., & Mohammadzadeh, K. (2022). Preparation of monolithic amorphous silica aerogel through promising valorization of silicomanganese slag. *Journal of Non-crystalline Solids, 586*, Article 121561. https://doi.org/10.1016/j.jnoncrysol.2022.121561

Nath, S. K., & Kumar, S. (2019). Influence of granulated silico-manganese slag on compressive strength and microstructure of ambient cured alkali-activated fly ash binder. *Waste and Biomass Valorization, 10*, 2045–2055. https://doi.org/10.1007/s12649-018-0213-1

Pereira, M. A., Vasconcelos, D. C. L., & Vasconcelos, W. L. (2019). Synthetic aluminosilicates for geopolymer production. *Materials Research, 22*, Article e20180508. https://doi.org/10.1590/1980-5373-mr-2018-0508

Piriya, R. S., Jayabalakrishnan, R. M., Maheswari, M., Boomiraj, K., & Oumabady, S. (2023). Comparative adsorption study of malachite green dye on acid-activated carbon. *International Journal of Environmental Analytical Chemistry, 103*, 16–30.

Rehman, U., Jacob, J., Mahmood, K., Ali, A., Ashfaq, A., Amin, N., Ikram, S., Ahmad, W., & Hussain, S. (2019). Direct growth of ZnSnO nano-wires by thermal evaporation technique for thermoelectric applications. *Physica B: Condensed Matter, 570*, 232–235. https://doi.org/10.1080/03067319.2020.1849667

Sartape, A. S., Mandhare, A. M., Jadhav, V. V., Raut, P. D., Anuse, M. A., & Kolekar, S. S. (2017). Removal of malachite green dye from aqueous solution with adsorption technique using Limonia acidissima (wood apple) shell as low cost adsorbent. *Arabian Journal of Chemistry, 10*, S3229–S3238. https://doi.org/10.1016/j.arabjc.2013.12.019

Shalygin, A. S., Kozhevnikov, I. V., Gerasimov, E. Y., Andreev, A. S., Lapina, O. B., & Martyanov, O. N. (2017). The impact of Si/Al ratio on properties of aluminosilicate aerogels. *Microporous and Mesoporous Materials, 251*, 105–113. https://doi.org/10.1016/j.micromeso.2017.05.053

Tavandashti, P., Zandrahimi, M., & Akbari, B. (2009). Agglomeration assessment of nano-sized alumina powders. *Iranian Journal of Materials Science and Engineering, 6*, 15–19.

Thakur, S., Katyal, S. C., & Singh, M. (2009). Structural and magnetic properties of nano nickel–zinc ferrite synthesized by reverse micelle technique. *Journal of Magnetism and Magnetic Materials, 321*, 1–7. https://doi.org/10.1016/j.jmmm.2008.07.009

Tyson, B. M., Abu Al-Rub, R. K., Yazdanbakhsh, A., & Grasley, Z. (2011). A quantitative method for analyzing the dispersion and agglomeration of nano-particles in composite materials. *Composites Part B: Engineering, 42*, 1395–1403. https://doi.org/10.1016/j.compositesb.2011.05.020

Ullah, S., Ur Rahman, A., Ullah, F., Rashid, A., Arshad, T., Viglašová, E., Galamboš, M., Mahmoodi, N. M., & Ullah, H. (2021). Adsorption of malachite green dye onto mesoporous natural inorganic clays: Their equilibrium isotherm and kinetics studies. *Water, 13*, 965. https://doi.org/10.3390/w13070965

Zhang, Y. J., He, P. Y., Chen, H., & Liu, L. C. (2018). Green transforming metallurgical residue into alkali-activated silicomanganese slag-based cementitious material as photocatalyst. *Materials, 11*, 1773. https://doi.org/10.3390/ma11091773

Zheng, G., Cui, X., Zhang, W., Tong, Z., & Li, F. (2012). Preparation of nano-sized Al_2O_3–SiO_2 powder by sol–gel plus azeotropic distillation method. *Particuology, 10*, 42–45. https://doi.org/10.1016/j.partic.2011.07.007

Zhuang, X. Y., Chen, L., Komarneni, S., Zhou, C. H., Tong, D. S., Yang, H. M., Yu, W. H., & Wang, H. (2016). Fly ash-based geopolymer: Clean production, properties and applications. *Journal of Cleaner Production, 125*, 253–267. https://doi.org/10.1016/j.jclepro.2016.03.019